Research Square

Preprints are preliminary reports that have not undergone peer review.
They should not be considered conclusive, used to inform clinical practice,
or referenced by the media as validated information.

# Annexin A4 mechanically stabilizes the nuclear envelope following membrane rupture

**Jesper Nylandsted**

jnl@cancer.dk

Danish Cancer Institute https://orcid.org/0000-0001-6474-5093

**Stine Sønder**

Danish Cancer Institute

**Ellen Pørtner**

University of Southern Denmark https://orcid.org/0000-0001-6360-1186

**Anna Mularski**

University of Southern Denmark

**Srinivasa Kolapalli**

Danish Cancer Institute https://orcid.org/0000-0003-2209-2519

**Younes Baroojii**

University of Copenhagen https://orcid.org/0000-0002-0907-9339

**Jonathan Bao**

Danish Cancer Institute

**Kathrine Christensen**

University of Southern Denmark

**Cristina Almeida**

Danish Cancer Institute

**Asger Lodal**

Danish Cancer Institute

**Malene Ebstrup**

Danish Cancer Institute

**Theresa Louise Boye**

Danish Cancer Society Research Center

**Apolinar Maya-Mendoza**

Danish Cancer Society Research Centre https://orcid.org/0000-0001-7452-9896

**Koji Kinoshita**

University of Southern Denmark

**Katarina Wolf**

Nijmegen Centre for Molecular Life Sciences (NCMLS) Netherlands

**Poul Martin Bendix**

University of Copenhagen

**Adam Simonsen**

University of Southern Denmark

**Article**

**Keywords:**

**Posted Date:** November 11th, 2026

**DOI:** https://doi.org/10.21203/rs.3.rs-11635905/v1

**License:** This work is licensed under a Creative Commons Attribution 4.0 International License.
Read Full License

**Additional Declarations:** There is **NO** Competing Interest.

# Annexin A4 mechanically stabilizes the nuclear envelope following membrane rupture

**Authors:** Stine Lauritzen Sønder[1], Ellen Juel Pørtner[2], Anna Mularski[2], Srinivasa Prasad Kolapalli[1], Younes Farhangi Barooji[3], Jonathan Chua Wei Bao[1], Kathrine Christensen[2], Cristina Almeida[1], Asger Lodal[1], Malene Laage Ebstrup[1], Theresa Louise Boye[1], Apolinar Maya-Mendoza[1], Koji Kinoshita[4], Katarina Wolf[5], Poul Martin Bendix[3], Adam Cohen Simonsen[2], and Jesper Nylandsted[1, 4*]

[1]Danish Cancer Institute, Strandboulevarden 49, 2100, Copenhagen, Denmark.
[2]Department of Physics, Chemistry and Pharmacy, University of Southern Denmark, Campusvej 55, DK-5230 Odense M. Denmark.
[3]Niels Bohr Institute, University of Copenhagen, Jagtvej 132, DK-2200 København N, Copenhagen, Denmark
[4]Department of Molecular Medicine, University of Southern Denmark, Campusvej 55, DK-5230 Odense M. Denmark.
[5]Department of Medical BioSciences, Radboud Institute for Molecular Life Sciences, Radboud University Medical Center, Geert Grooteplein Zuid 28, 6525 GA Nijmegen, The Netherlands.

*Correspondence to JN: jnl@cancer.dk

**Keywords:** Nuclear envelope, Annexins, Membrane stabilization, Membrane mechanics, Nuclear integrity, Annexin.

## Abstract

The nuclear envelope (NE) preserves genome integrity by maintaining nuclear compartmentalization but is susceptible to rupture under mechanical stress. Although mechanisms that restore NE continuity have been identified, how damaged nuclear membranes are mechanically stabilized remains poorly understood. Here, we identify annexin A4 (ANXA4) as a $Ca^{2+}$-dependent regulator of NE stability. Using live-cell imaging and targeted membrane injury, we show that ANXA4 rapidly accumulates at damaged regions of the NE, where its sustained association requires $Ca^{2+}$ binding and trimer formation. Functionally, ANXA4 limits the loss of nuclear compartmentalization following injury, including under conditions of increased nuclear fragility. Atomic force microscopy of isolated nuclei reveals that ANXA4 reduces nuclear surface roughness and increases the apparent stiffness of the nuclear envelope, while experiments with reconstituted membranes demonstrate that ANXA4 directly enhances resistance to mechanical rupture. Together, these findings support a model in which ANXA4 provides an early mechanical defense against nuclear membrane damage, revealing membrane reinforcement as a protective mechanism that helps preserve nuclear compartmentalization following rupture.

## Introduction

In eukaryotic cells, the nuclear envelope (NE) forms a critical barrier that physically separates chromosomal DNA from the cytoplasm, thereby maintaining nuclear compartmentalization and protecting genome integrity. The NE comprises an outer and inner nuclear membrane that converge at nuclear pore complexes (NPCs), highly specialized structures that regulate bidirectional molecular trafficking between the nucleus and cytoplasm[1,2]. The inner nuclear membrane is further supported by the nuclear lamina, a filamentous meshwork of intermediate filament proteins known as lamins, which provides mechanical stability to the nucleus[3].

Mechanical deformation or chemical stress can compromise NE integrity, resulting in transient rupture events that disrupt nuclear compartmentalization, permit uncontrolled exchange between nuclear and cytoplasmic compartments[4], and promote DNA double-strand breaks[5,6]. Such rupture events are particularly prevalent during confined cell migration, where extreme nuclear deformation can lead to repeated loss of NE integrity and contribute to genomic instability, including in metastatic cancer cells[5,6].

Despite these potentially deleterious consequences, cells can survive repeated NE rupture events by rapidly restoring the nuclear permeability barrier. Interphase NE repair involves barrier-to-autointegration factor (BAF), which rapidly accumulates at rupture sites and recruits transmembrane LEM-domain proteins and nuclear membranes to the damaged region[7,8]. Among these proteins, LEMD2 interacts with CHMP7 and promotes recruitment of the Endosomal Sorting Complex Required for Transport III (ESCRT-III) machinery, which mediates membrane remodeling and sealing at the NE[5-9]. However, the mechanisms governing NE repair are not fully resolved. BAF and LEM-domain proteins contribute to restoration of the nuclear permeability barrier, particularly following larger ruptures, whereas ESCRT-III appears dispensable for repair under some conditions[7,8]. Thus, additional mechanisms are likely to operate alongside canonical repair machinery to stabilize damaged nuclear membranes and facilitate restoration of NE integrity.

Annexins (ANXAs) are a family of $Ca^{2+}$-dependent phospholipid-binding proteins (ANXA1–A11 and ANXA13 in mammals), several of which are well-established mediators of plasma membrane repair[10]. Upon plasma membrane injury, extracellular $Ca^{2+}$ influx triggers their rapid recruitment to damaged membrane. Through their conserved C-terminal domains,

annexins bind anionic phospholipids and promote membrane remodeling through lipid aggregation, membrane fusion and curvature induction[11-15]. Our previous work has demonstrated that several annexins, including ANXA1, ANXA2 and ANXA4–A7, induce membrane curvature and, through coordinated activities, contribute to efficient plasma membrane repair[13,14,16]. Notably, ANXA4 and ANXA5 preferentially localize to highly curved membrane regions, including free membrane edges at rupture sites, consistent with a capacity to stabilize membrane discontinuities[13,15].
Annexins have also been reported to translocate to the NE in response to elevated cytoplasmic $Ca^{2+}$ levels, but their functional role at the NE remains poorly defined[17]. Given their rapid $Ca^{2+}$-dependent recruitment to damaged membranes and their ability to alter membrane organization and mechanics, annexins are therefore plausible candidates for an early membrane-stabilizing response to NE rupture.

Here, we investigated whether annexins contribute directly to stabilization of the damaged NE. Combining live-cell imaging and targeted membrane injury with functional measurements of nuclear integrity and atomic force microscopy (AFM) of isolated nuclei and reconstituted membranes, we identify ANXA4 as a $Ca^{2+}$-dependent regulator of NE stability. ANXA4 is rapidly recruited to sites of NE damage, where $Ca^{2+}$ binding and trimerization promote its stable membrane association. ANXA4 preserves nuclear compartmentalization following rupture and directly alters the mechanical properties of isolated nuclei and reconstituted membranes, increasing membrane resistance to mechanical failure. Together, our findings identify ANXA4-mediated membrane reinforcement as an early protective response to NE damage that operates alongside established nuclear envelope repair mechanisms.

## Results

### Differential recruitment of ANXA4 and ANXA6 to the nuclear envelope following injury

To induce localized and spatially confined damage to the NE, we employed UV laser ablation, enabling precise disruption of membranes in living cells. This approach allowed us to reproducibly induce transient rupture of the NE while simultaneously causing localized plasma membrane damage, enabling real-time monitoring of the immediate cellular response with high temporal resolution. Given the membrane-remodeling and stabilizing activities of

annexins during plasma membrane injury, we investigated whether ANXA4 and ANXA6 are recruited to the NE following damage. To this end, we co-expressed ANXA6 fused to TurboGFP (ANXA6–tGFP) together with the NE marker Lamin B1 fused to tdTomato (tdTomato–Lamin B1) in MCF-7 cells. Laser-induced injury resulted in plasma membrane disruption, as indicated by ANXA6–tGFP accumulation, accompanied by a marked increase in perinuclear signal at the NE. Magnified views of the same images showed that ANXA6–tGFP did not colocalize with Lamin B1 but instead formed a closely apposed signal adjacent to the Lamin B1–defined boundary, consistent with localization to its outer surface (Fig. 1A, B). Notably, ANXA6–tGFP redistributed around the entire NE, forming a continuous perinuclear signal encircling the nucleus (Fig. 1A).

In parallel, UV laser injury experiments revealed distinct recruitment patterns of ANXA4–tGFP and ANXA6–tGFP at the nuclear envelope. Whereas ANXA6–tGFP showed a relatively uniform perinuclear distribution, ANXA4–tGFP accumulated more prominently at the Lamin B1–defined nuclear boundary and was preferentially localized to the injured hemisphere, resulting in a polarized recruitment pattern (Fig. 1C). Consistent with this spatial distribution, fluorescence intensity measurements confirmed greater enrichment of ANXA4–tGFP at the nuclear envelope compared with ANXA6–tGFP (Fig. 1B, D).

To determine whether this response also occurs for endogenous ANXA4 and following mechanical stress, cells were compressed between two glass coverslips and subsequently immunostained using an ANXA4-specific antibody. Mechanical compression resulted in a pronounced redistribution of endogenous ANXA4 to the nuclear periphery, with strong enrichment at the NE (Fig. 1E). Together, these results show that ANXA4 and ANXA6 are recruited to the NE following injury, with ANXA4 exhibiting a stronger and more spatially restricted enrichment. Moreover, the recruitment of endogenous ANXA4 in response to mechanical compression indicates that ANXA4 accumulation at the NE is not restricted to ectopically expressed ANXA4 or UV laser-induced injury.

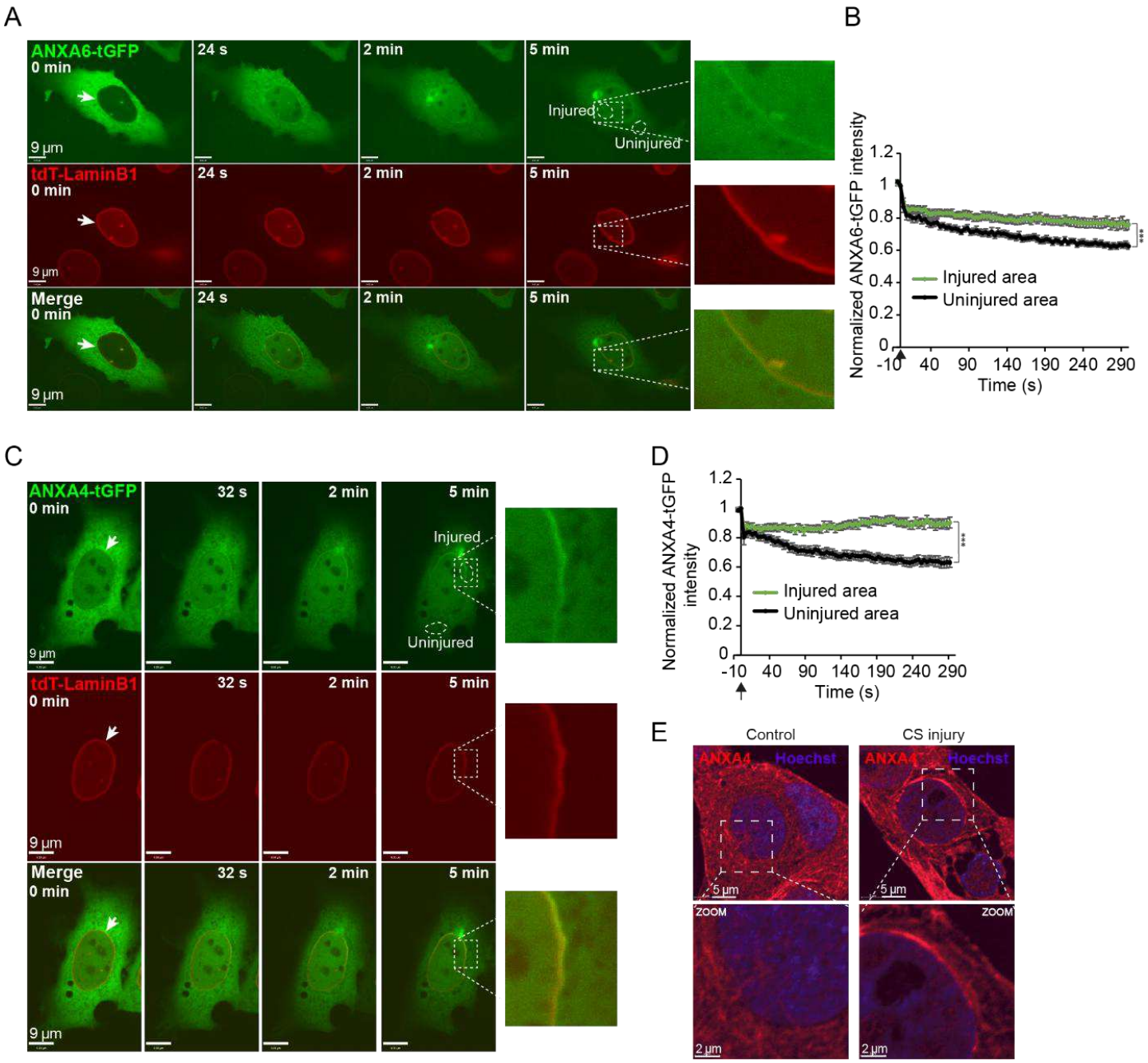



**Fig. 1. Injury induces recruitment of ANXA6 and ANXA4 to the nuclear envelope with distinct spatial patterns.**

(**A** and **B**) Representative sequential images of MCF7 cells co-expressing ANXA6–tGFP and tdTomato–Lamin B1 following laser-induced injury (white arrow indicates injury site). Zoomed-in views highlight ANXA6 recruitment to the nuclear envelope, which appears distributed around the entire nuclear perimeter. White circles indicate regions used for fluorescence intensity quantification. (**B**) Quantification of ANXA6–tGFP fluorescence intensity at the nuclear envelope in injured regions compared to uninjured control regions. Data are shown as mean ± SEM (15 cells from three independent experiments; paired t test of AUC values). Black arrow indicates time of injury. (**C** and **D**) Representative sequential images of MCF7 cells co-expressing ANXA4–tGFP and tdTomato–Lamin B1 following laser-induced injury (white arrow indicates injury site). Zoomed-in views highlight ANXA4 recruitment to the nuclear envelope, which is predominantly restricted to the injured hemisphere, giving rise to a polarized perinuclear signal. White circles indicate regions used for fluorescence intensity quantification. (**D**) Quantification of ANXA4–tGFP fluorescence intensity at

the nuclear envelope in injured regions compared to uninjured control regions. Data are shown as mean ± SEM (nine cells from three independent experiments; paired t test of AUC values). Black arrow indicates time of injury. ***P ≤ 0.001. (**E**) Representative fluorescence images showing endogenous ANXA4 localization in control cells and following mechanical compression between two glass coverslips. Cells were fixed after compression and immunostained with an ANXA4-specific antibody.

## $Ca^{2+}$ binding and trimerization govern ANXA4 recruitment and retention at the damaged nuclear envelope

Given the pronounced and polarized enrichment of ANXA4 at the NE, we next investigated the molecular determinants governing its recruitment. Wild-type and mutant ANXA4–tRFP constructs were reintroduced into MCF7 CRISPR ANXA4 knockout cells (MCF7 CRISPR ANXA4KO) co-expressing eGFP-tagged NUP153, a nuclear pore complex protein, as an NE marker (Fig. 2). Following laser injury, wild-type ANXA4–tRFP rapidly accumulated at the NE, with pronounced and polarized enrichment evident within ~2 min and closely coinciding with the eGFP–NUP153-defined nuclear boundary (Fig. 2A, Movie S1). Comparable expression of wild-type ANXA4–tRFP and the $Ca^{2+}$-binding–deficient mutant ANXA4$Ca^{2+}$–RFP was confirmed by immunoblotting, whereas the trimerization-deficient mutant ANXA4TriMut–RFP showed slightly lower expression (Fig. 2B). Quantification of fluorescence intensity at the injured NE relative to uninjured regions confirmed robust enrichment of wild-type ANXA4–tRFP following injury (Fig. 2C).

In contrast, ANXA4$Ca^{2+}$–RFP showed minimal accumulation at the NE and remained predominantly cytosolic, with no apparent translocation to the damaged region (Fig. 2D, Movie S2). Accordingly, fluorescence intensity measurements provided no evidence of sustained injury-induced enrichment at the NE (Fig. 2E). ANXA4TriMut–RFP displayed a distinct response: although a transient increase in perinuclear signal was observed following injury, this accumulation was not maintained, and the protein rapidly redistributed away from the nuclear boundary (Fig. 2F, Movie S3). Quantification likewise showed that ANXA4TriMut–RFP did not exhibit the sustained NE enrichment observed for wild-type ANXA4–tRFP (Fig. 2G). Together, these findings support a two-step mechanism in which $Ca^{2+}$ binding enables ANXA4 recruitment to the damaged membrane, whereas trimerization promotes its stable membrane association.

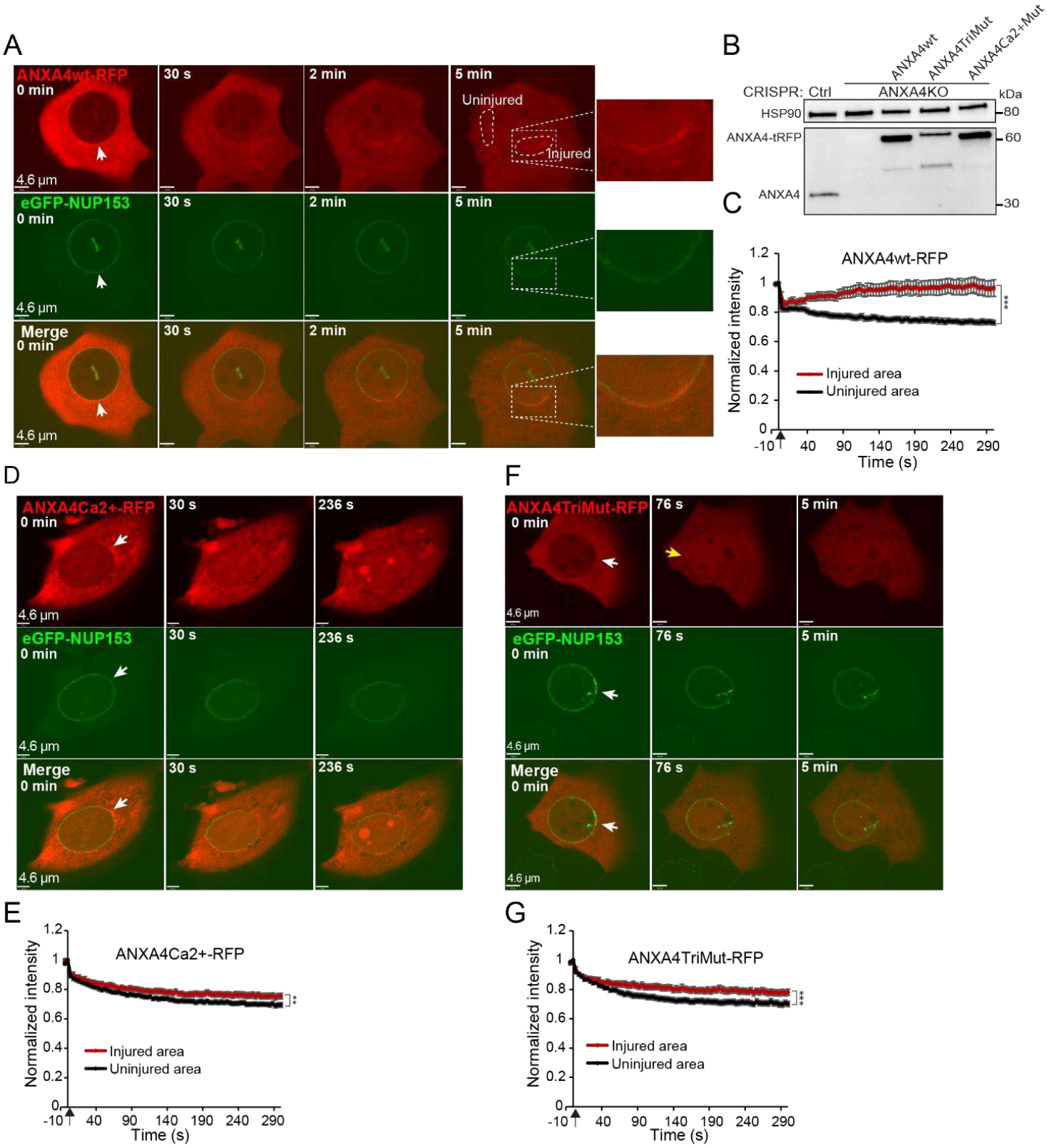



**Fig. 2. ANXA4 recruitment to the nuclear envelope requires $Ca^{2+}$ binding and trimer formation.** **(A,D,F)** Representative time-lapse images of MCF7 CRISPR ANXA4 knockout (ANXA4KO) cells co-expressing eGFP–NUP153 and either ANXA4wt–RFP (A), the $Ca^{2+}$-binding–deficient mutant ANXA4$Ca^{2+}$Mut–RFP (D), or the trimerization-deficient mutant ANXA4TriMut–RFP (F) following

laser-induced nuclear envelope injury (white arrows indicate injury sites). Zoomed-in images in (A) show recruitment of ANXA4wt–RFP to the injured nuclear envelope (See also Movies S1-S3). White circles indicate regions used for fluorescence quantification. Yellow arrows indicate ANXA4TriMut–RFP translocation. Scale bars, 4.6 μm. **(B)** Representative immunoblot of lysates from MCF7 CRISPR control (Ctrl) and ANXA4KO cells following re-expression of ANXA4wt–RFP, ANXA4TriMut–RFP, or ANXA4Ca$^{2+}$Mut–RFP. Blots were probed with antibodies against ANXA4 and HSP90 (loading control). Original unedited blots are shown in Fig. S1A. **(C, E, G)** Quantification of fluorescence intensity at the injured nuclear envelope for ANXA4wt–RFP (C), ANXA4Ca$^{2+}$Mut–RFP (**E**), and ANXA4TriMut–RFP (**G**) following laser-induced injury. Fluorescence intensities were normalized to uninjured cytoplasmic regions. Data represent mean ± SEM from a minimum of 29 cells per condition pooled from three independent experiments. Statistical significance was assessed using paired *t* tests of area-under-the-curve (AUC) values. **P ≤ 0.01; ***P ≤ 0.001.

**ANXA4 recruitment to the damaged nuclear envelope depends on Ca$^{2+}$ influx**

Having established that ANXA4 recruitment to the NE depends on Ca$^{2+}$ binding and trimer formation, we next asked whether damage to the NE alone is sufficient to trigger ANXA4 translocation, or whether concomitant plasma membrane disruption is required. To this end, we used optical tweezers in combination with gold nanoparticles to induce spatially confined, heat-mediated damage at defined subcellular locations[18,19]. NE integrity was monitored using a nuclear localization signal reporter (NLS–GFP), which redistributes from the nucleus to the cytoplasm upon NE disruption, while plasma membrane permeabilization was assessed using an impermeable Alexa Fluor 647–conjugated dye that enters cells only upon plasma membrane rupture (Fig. 3A).

Localized damage to the NE alone, as indicated by NLS–GFP leakage in the absence of Alexa Fluor 647 uptake, was not sufficient to induce ANXA4–tRFP recruitment. In contrast, conditions in which both NE disruption and plasma membrane permeabilization occurred resulted in robust ANXA4–tRFP translocation to the NE (Fig. 3B–C). Together, these findings indicate that ANXA4 recruitment to the damaged NE requires a sufficiently strong Ca$^{2+}$ signal. Under our experimental conditions, NE disruption alone was insufficient to induce detectable ANXA4 accumulation, whereas accompanying plasma membrane disruption enabled ANXA4 recruitment, consistent with extracellular Ca$^{2+}$ influx providing the Ca$^{2+}$ levels required for ANXA4 membrane engagement.

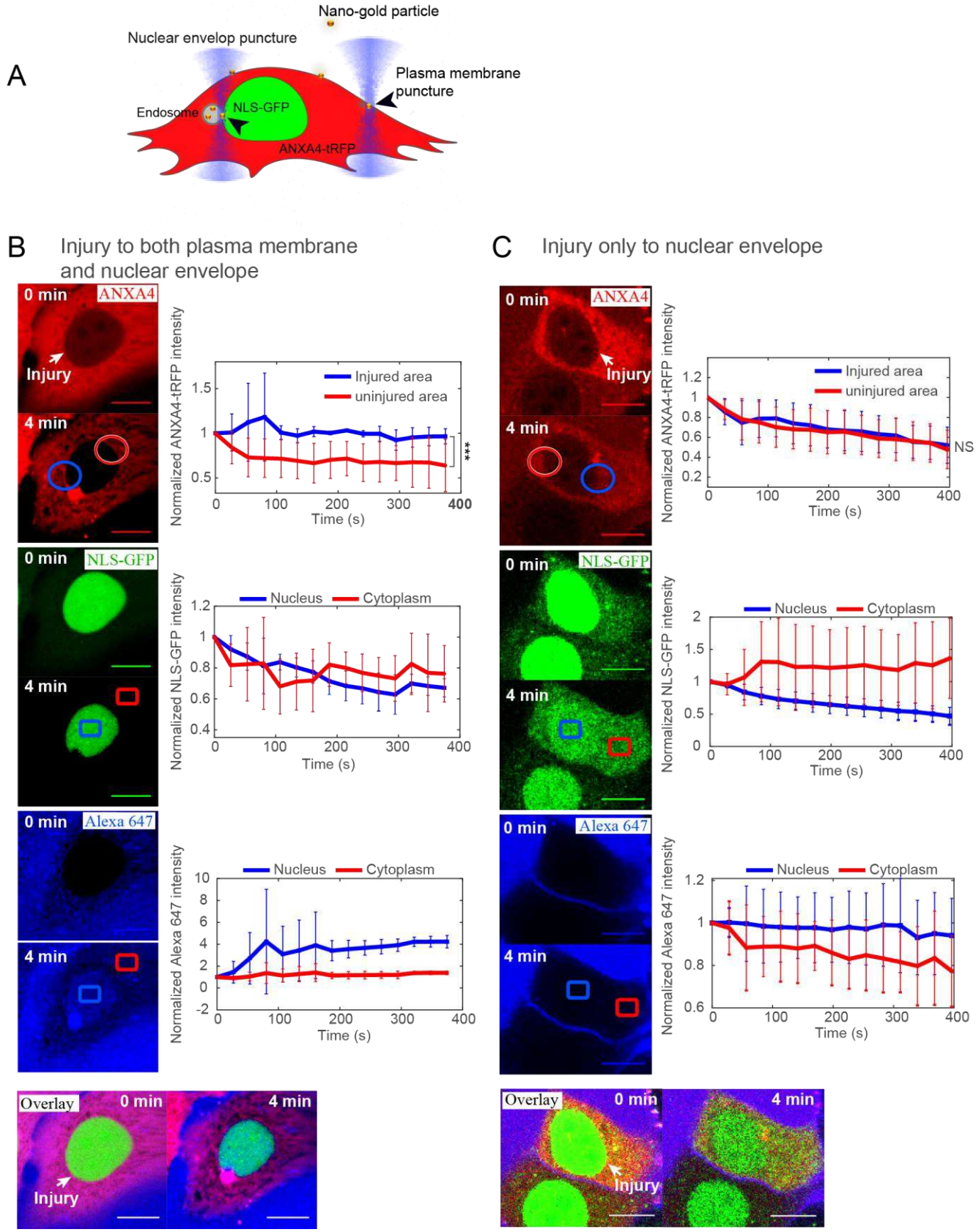



**Fig. 3. ANXA4 recruitment to the damaged nuclear envelope depends on plasma membrane disruption.** (**A**) Schematic of the experimental setup. Optical tweezers were used to heat internalized gold nanoparticles to induce localized damage at defined subcellular regions. Nuclear envelope

disruption was monitored by redistribution of NLS–GFP, whereas plasma membrane permeabilization was assessed by uptake of an impermeable Alexa Fluor 647 dye. (**B**) Combined plasma membrane and nuclear envelope damage induces ANXA4 recruitment to the nuclear envelope. Representative images of MCF7 cells expressing ANXA4–tRFP (red), NLS–GFP (green), and membrane impermeable Alexa Fluor 647 dye (blue) before (0 min) and after (4 min) injury (arrow). ANXA4–tRFP accumulates at the nuclear envelope, accompanied by NLS–GFP leakage and intracellular Alexa Fluor 647 signal. Quantification shows increased ANXA4–tRFP intensity at the injured nuclear envelope compared to uninjured regions. (**C**) Nuclear envelope damage alone is insufficient to induce ANXA4 recruitment. NLS–GFP redistribution indicates nuclear envelope disruption in the absence of Alexa Fluor 647 uptake, confirming an intact plasma membrane. Data are normalized to pre-injury levels and shown as mean ± SEM. Statistics: paired t-test, $P \leq 0.001$ (***). NS: not significant.

**ANXA4 stabilizes the nuclear envelope in a trimerization-dependent manner**

We next investigated whether ANXA4 contributes to the maintenance of NE integrity following injury. MCF7 CRISPR ANXA4KO cells were reconstituted with either ANXA4–tRFP or control tRFP (Fig. 4A) and subjected to laser-induced NE injury in the presence of membrane-impermeable Hoechst dye. NE rupture resulted in rapid accumulation of Hoechst within the nucleus, reflecting loss of compartmentalization and increased nuclear permeability. Notably, cells expressing ANXA4–tRFP exhibited significantly reduced nuclear Hoechst accumulation compared with control cells (Fig. 4B, C), indicating that ANXA4 limits dye influx and promotes preservation of NE integrity following injury.

It should be noted, however, that this assay reports overall cellular barrier function and therefore cannot distinguish between contributions of plasma membrane repair and NE repair/stabilization to the observed reduction in nuclear Hoechst accumulation. To specifically assess NE compartmentalization independently of plasma membrane permeability, we next monitored NLS–GFP redistribution following laser-induced NE injury. For these experiments, laser exposure was adjusted to induce limited NE disruption while avoiding extensive nuclear damage, thereby allowing differences in the preservation of nuclear compartmentalization to be resolved.

MCF7 CRISPR ANXA4KO cells expressing wild-type ANXA4–tRFP, Ctrl–tRFP, or the trimerization-deficient mutant ANXA4TriMut–tRFP were co-transfected with NLS–GFP and subjected to laser-induced NE injury. Imaging was focused primarily on the redistribution of NLS–GFP as a readout of NE integrity. Whereas NLS–GFP remained largely confined to the

nucleus in cells expressing wild-type ANXA4, cells expressing Ctrl–tRFP or ANXA4TriMut–tRFP showed increased redistribution of NLS–GFP from the nucleus following injury (Fig. 4D). Quantification of nuclear NLS–GFP fluorescence confirmed a significantly greater loss of nuclear signal in Ctrl–tRFP- and ANXA4TriMut–tRFP-expressing cells compared with cells expressing wild-type ANXA4–tRFP (Fig. 4E). Together, these results indicate that ANXA4 promotes the preservation of nuclear compartmentalization following NE injury and that this protective effect depends on its ability to form trimers.

To determine whether this phenotype was maintained under conditions of increased nuclear fragility, we next employed mouse embryonic fibroblasts (MEFs) with deletion of Lamin A[20,21], which renders the NE more susceptible to mechanical stress and rupture[22]. Loss of Lamin A expression was confirmed by immunoblotting (Fig. 4F). Lamin A-deficient MEFs expressing either ANXA4–tRFP or ANXA4TriMut–RFP were co-transfected with NLS–GFP and subjected to laser-induced NE injury. Consistent with the findings in MCF7 cells, NLS–GFP remained largely confined to the nucleus in cells expressing wild-type ANXA4, whereas cells expressing ANXA4TriMut–RFP displayed rapid redistribution of NLS–GFP into the cytoplasm following injury (Fig. 4G). Quantification of nuclear NLS–GFP fluorescence revealed a significantly greater loss of nuclear signal in cells expressing ANXA4TriMut–RFP compared with cells expressing wild-type ANXA4–tRFP (Fig. 4F).
Together, these findings demonstrate that ANXA4 protects NE integrity following injury. The inability of the trimerization-deficient ANXA4TriMut mutant to confer similar protection in either MCF7 cells or Lamin A-deficient MEFs further identifies trimer formation as a critical requirement for ANXA4-mediated stabilization of the damaged NE.

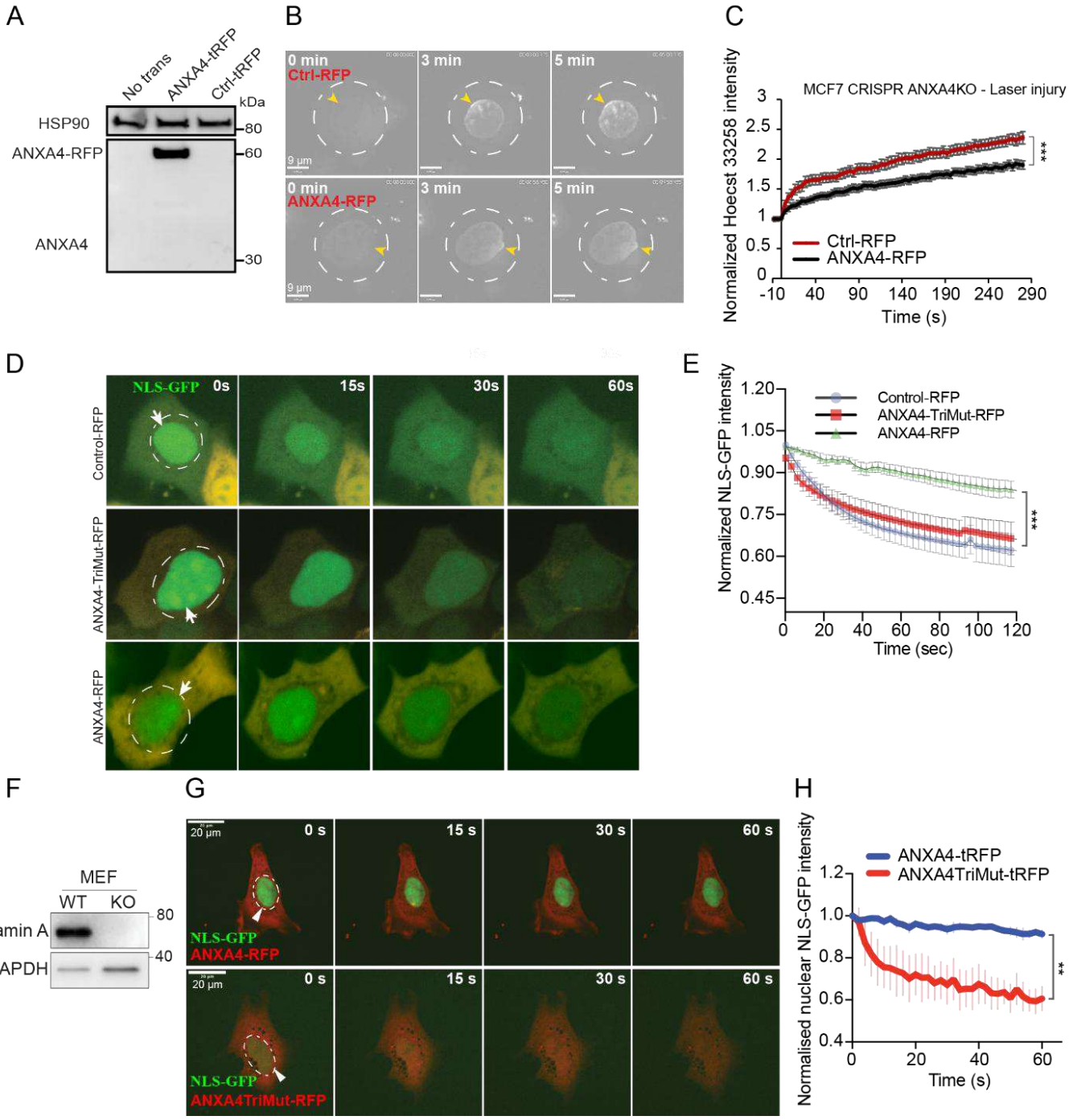



**Fig. 4. ANXA4 stabilizes the nuclear envelope in a trimerization-dependent manner.**

(**A**) Immunoblot showing ANXA4–tRFP expression following reintroduction into MCF7 CRISPR ANXA4 knockout cells. HSP90 serves as a loading control. Original unedited blots are shown in Fig. S1B. (**B**) Representative time-lapse images of MCF7 CRISPR ANXA4 knockout cells expressing Ctrl–tRFP or ANXA4–tRFP in the presence of a membrane-impermeable Hoechst dye before (0 min) and after laser-induced injury. Nuclear Hoechst accumulation reflects loss of membrane integrity. (**C**) Quantification of normalized nuclear Hoechst fluorescence over time following injury. Data are presented as mean ± SEM from three experiments. (**D**) Representative time-lapse fluorescence images of MCF7 CRISPR ANXA4 knockout cells co-expressing NLS–GFP and either Ctrl–tRFP, wild-type ANXA4–tRFP, or the trimerization-deficient ANXA4TriMut–tRFP following laser-induced NE injury. Laser exposure was adjusted to induce limited NE disruption while avoiding extensive nuclear damage. Redistribution of NLS–GFP from the nucleus to the cytoplasm was monitored as a readout of NE integrity. (**E**) Corresponding quantification of normalized nuclear NLS–GFP fluorescence over

time following NE injury. Data are presented as mean ± SEM. (**F**) Immunoblot confirming loss of Lamin A in the Lamin A knockout MEFs. GAPDH serves as a loading control. (**G**) Representative time-lapse fluorescence images of Lamin A-deficient MEFs co-expressing NLS–GFP and either wild-type ANXA4–tRFP (top) or ANXA4TriMut–tRFP (bottom) before and after laser-induced NE injury. (**H**) Corresponding quantification of normalized nuclear NLS–GFP fluorescence over time following injury. Data are presented as mean ± SEM at least three experiments. Statistical analysis: unpaired t test with Welch's correction. $P \leq 0.01$ (**), and $P \leq 0.001$ (***).

**ANXA4 alters the mechanical properties of isolated nuclei**

Having established that ANXA4 stabilizes the NE in cells, we next asked whether membrane-associated ANXA4 alters the physical properties of isolated nuclei. To this end, nuclei were isolated from MCF7 CRISPR ANXA4 knockout cells and incubated with recombinant human ANXA4–sfGFP in the presence of $Ca^{2+}$ (Fig. 5A). Fluorescence microscopy confirmed robust binding of ANXA4–sfGFP to the surface of isolated nuclei, thereby providing a well-defined system to directly investigate whether ANXA4 alters the mechanical properties of the NE. AFM was subsequently employed to quantify the topography and nanomechanical properties of isolated nuclei. A schematic of the experimental setup is shown in Fig. 5B, and Fig. 5C illustrates a representative force–indentation experiment used to determine the apparent Young's modulus.

AFM imaging of control nuclei revealed a heterogeneous surface with pronounced nanoscale irregularities (Fig. 5D, F). In contrast, addition of recombinant ANXA4 resulted in a visibly smoother nuclear surface, consistent with reduced topographical heterogeneity (Fig. 5E). Quantitative analysis confirmed a significant reduction in surface roughness, as measured by root mean square (RMS) roughness, in ANXA4-treated nuclei compared to controls (Fig. 5F). In parallel, AFM-based nanoindentation measurements showed a significant increase in Young's modulus following ANXA4 addition, indicating increased apparent nuclear stiffness (Fig. 5G).

Together, these findings demonstrate that membrane-associated ANXA4 alters the physical properties of isolated nuclei, reducing surface irregularities and increasing apparent mechanical stiffness.

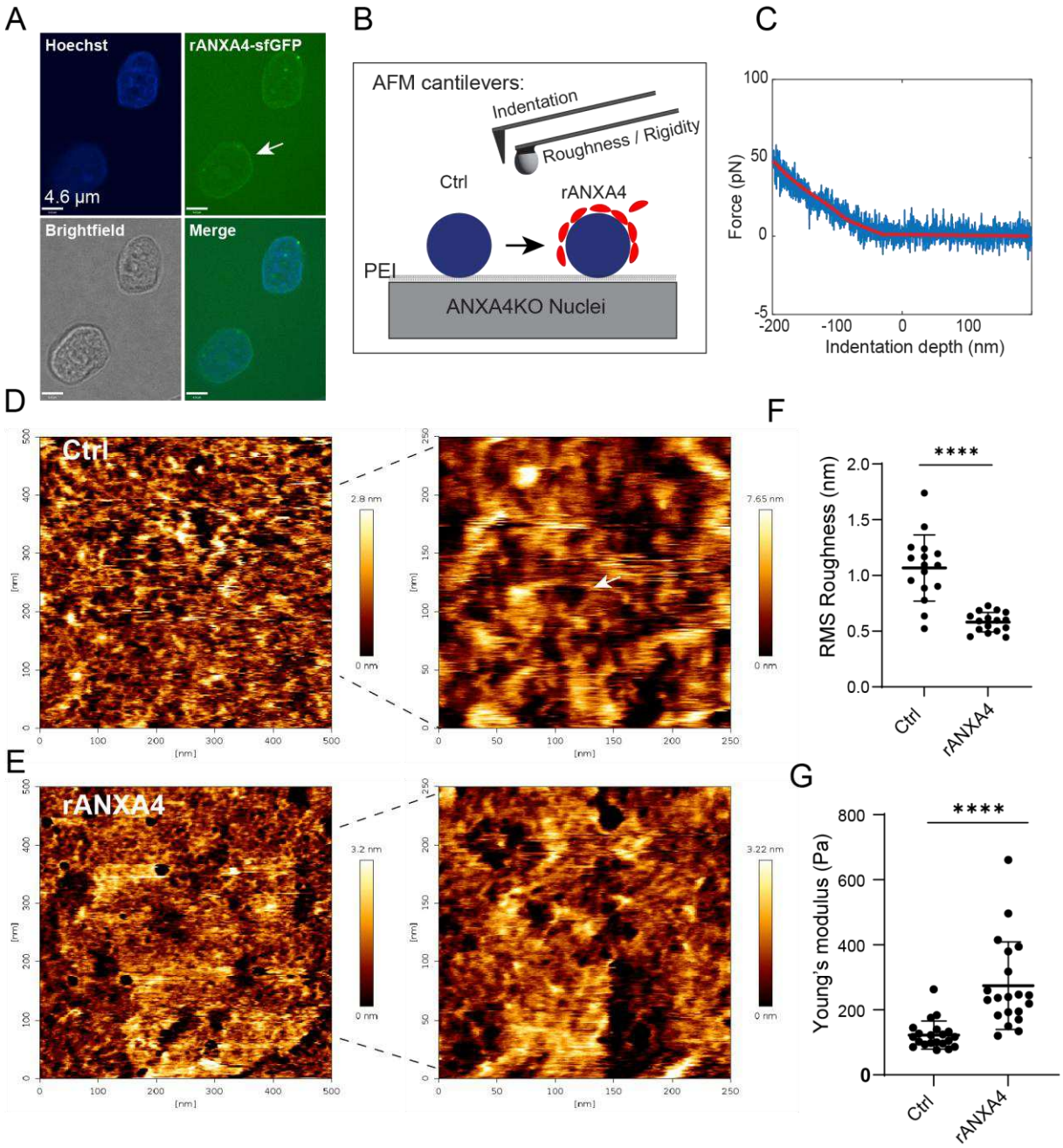



**Fig. 5. ANXA4 alters the mechanical properties of isolated nuclei.**
(**A**) Representative brightfield and fluorescence images of nuclei isolated from MCF7 CRISPR ANXA4KO cells incubated with recombinant human ANXA4–sfGFP (250 nM) in the presence of $Ca^{2+}$ (500 µM). Hoechst staining marks nuclei, and ANXA4–sfGFP signal shows binding to the nuclear surface. (**B**) Schematic of the atomic force microscopy (AFM) setup used to probe nuclear envelope topography and mechanical properties. (**C**) Representative force–indentation curve from AFM measurements on isolated nuclei. Force (pN) is plotted as a function of indentation depth (nm). The blue trace corresponds to the raw data and the red line indicates the fitted curve used for mechanical analysis. (**D** and **E**) Representative AFM topography images of isolated nuclei in the absence (control; **D**) or presence of recombinant ANXA4–sfGFP (**E**). Control nuclei exhibit pronounced nanoscale surface irregularities, whereas ANXA4-treated nuclei display a smoother surface topology. (**F**) Quantification of surface roughness, expressed as root mean square (RMS) roughness, showing reduced nuclear envelope roughness upon ANXA4 addition. A minimum of 16 nuclei per condition were analyzed across five independent experiments.
(**G**) Quantification of NE stiffness measured by AFM-based nanoindentation, expressed as Young's modulus, showing increased apparent nuclear stiffness following ANXA4 addition. A minimum of 20

nuclei per condition were analyzed from four independent experiments. Data are presented as mean ± SEM. Statistical significance was determined by Welch's t-test, ****$P \leq 0.0001$.

**ANXA4 increases membrane resistance to mechanical rupture**

To determine whether ANXA4 directly alters membrane mechanical properties, we used AFM force spectroscopy on supported lipid bilayers. In this assay, indentation of the bilayer by the AFM tip produces a characteristic force–distance curve, in which gradual membrane compression is followed by a sudden force drop corresponding to penetration of the bilayer core, referred to as the breakthrough force (Fig. 6A, B). Automated analysis of individual force curves allowed extraction of membrane thickness, compressed membrane thickness, breakthrough force and apparent Young's modulus.

Supported lipid bilayers composed of POPC/POPS were analyzed before and after incubation with recombinant ANXA4 protein. Addition of ANXA4 caused a significant increase in the force required to penetrate the membrane, with both 40 nM and 100 nM ANXA4 increasing the breakthrough force compared with control membranes (Fig. 6C). This effect was not accompanied by a proportional increase in compressed membrane thickness, which was only modestly affected (Fig. 6D). In contrast, the apparent uncompressed membrane thickness increased upon ANXA4 addition (Fig. 6E), consistent with ANXA4 binding to the membrane surface and/or promoting local membrane reorganization. These differences in measured thickness suggest a displacement of surface bound ANXA4 from underneath the colloidal probe tip during full compression, but not during initial contact.

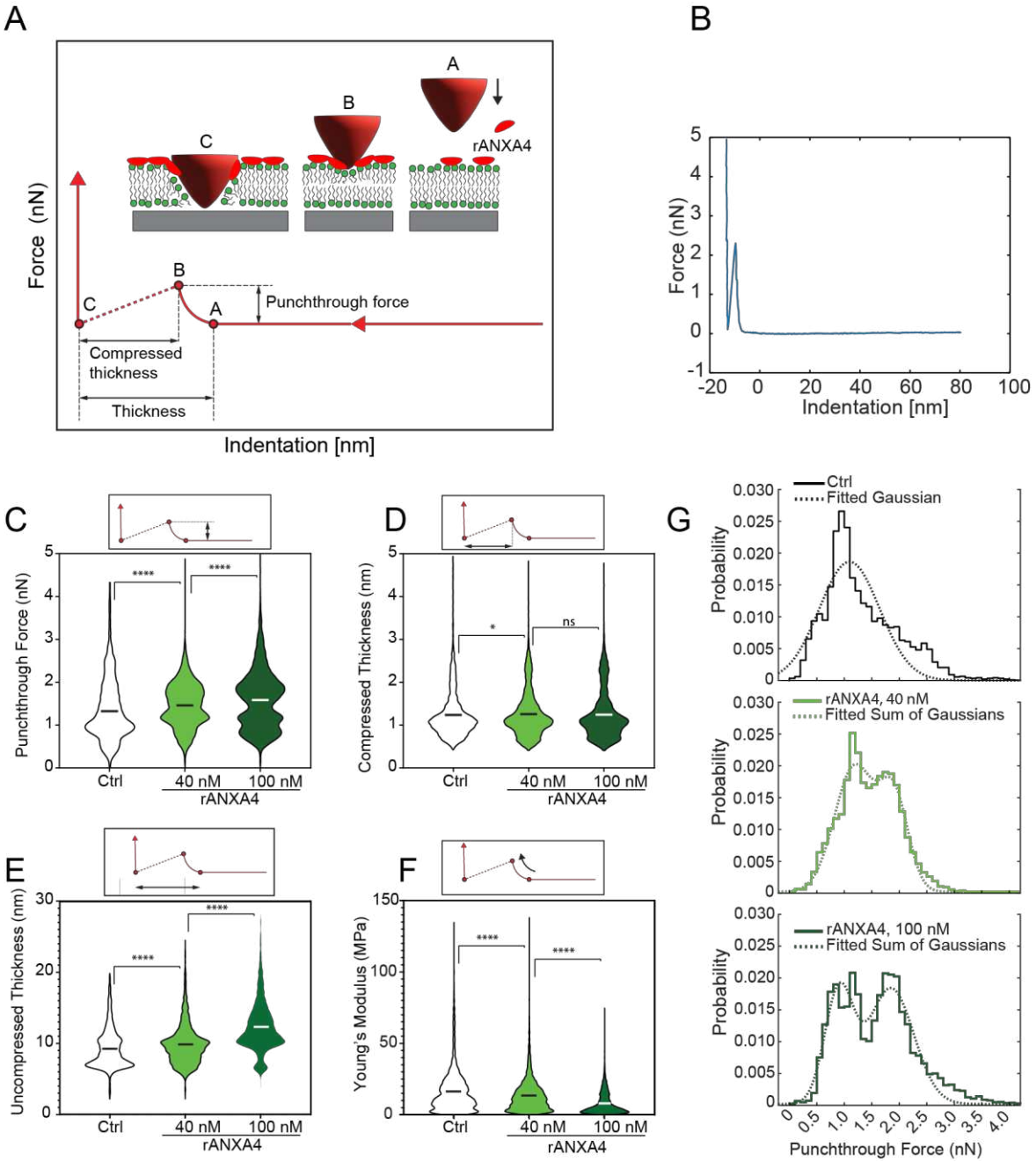



**Fig. 6. ANXA4 increases resistance of supported lipid bilayers to mechanical rupture.** (**A**) Schematic of AFM force spectroscopy measurements on POPC/POPS (9:1) supported lipid membrane bilayers. Indentation of the bilayer by the AFM cantilever results in membrane compression followed by bilayer punchthrough. Parameters extracted from force curves include punchthrough force, compressed thickness, and uncompressed thickness. (**B**) Representative force–indentation curve showing bilayer punchthrough. (C–F) Quantification of punchthrough force (**C**), compressed thickness (**D**), uncompressed thickness (**E**), and Young's modulus (**F**) for control membranes and membranes incubated with recombinant ANXA4 protein (40 or 100 nM). Horizontal lines indicate mean values; SEM was smaller than the line thickness. (**G**) Probability distributions of punchthrough force values for control and ANXA4-treated membranes. Gaussian fits yielded mean values of 1.09 nN for control; 1.19 and 1.91 nN for 40 nM ANXA4; and 0.90 and 1.85 nN for 100 nM ANXA4. ANXA4-treated distributions were vertically shifted for visualization. Data are from five independent experiments (control, n = 6006 force curves; ANXA4 40 nM, n = 7520; ANXA4 100 nM, n = 6559). $P < 0.05$; ****$P < 0.0001$; ns, not significant.

Interestingly, ANXA4 reduced the apparent Young's modulus of the supported bilayer (Fig. 6F), indicating that the increased breakthrough force does not simply reflect global membrane stiffening. Rather, ANXA4 appears to render the total bilayer + ANXA4 system more compressible compared to a pure bilayer, while increasing the bilayer resistance to rupture. Analysis of breakthrough-force distributions further revealed that control membranes displayed a largely unimodal distribution, whereas ANXA4-treated membranes showed bimodal distributions, with the higher force component emerging upon ANXA4 addition and having the largest proportion at 100 nM ANXA4 (Fig. 6G). This suggests that ANXA4 generates heterogeneous membrane states with regions of increased mechanical protection.

Together, these data demonstrate that ANXA4 directly reinforces lipid membranes against mechanical penetration. Rather than uniformly increasing bilayer stiffness, ANXA4 generates mechanically protected membrane states that increase the force required for membrane failure.

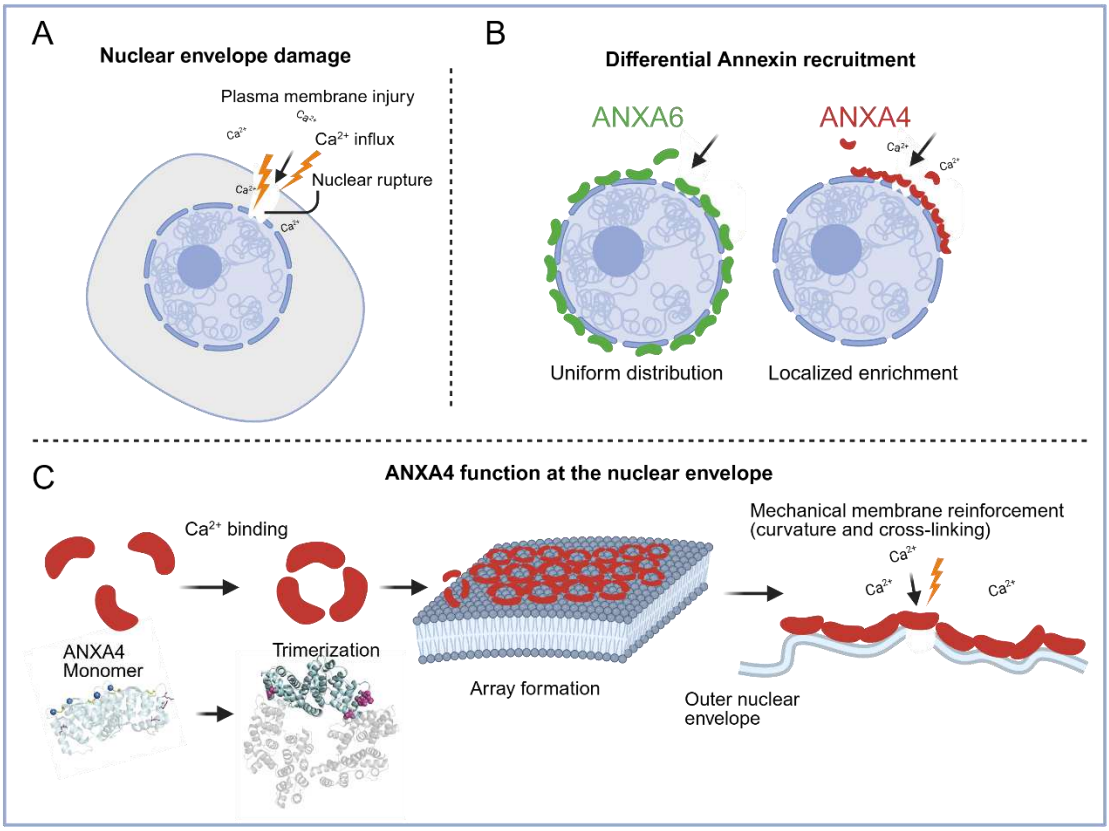



**Fig. 7. Model for ANXA4-mediated stabilization of the nuclear envelope.**
(**A**) Membrane injury results in nuclear envelope damage and an increase in cytoplasmic $Ca^{2+}$. (**B**) Elevated $Ca^{2+}$ promotes local recruitment of ANXA4 to the damaged nuclear membrane. $Ca^{2+}$ binding enables membrane recruitment, whereas trimerization promotes stable membrane association. Membrane-associated ANXA4 mechanically reinforces the damaged membrane, increasing its resistance to mechanical failure and thereby contributing to preservation of nuclear

compartmentalization. (**C**) Loss of $Ca^{2+}$ binding or trimerization compromises ANXA4-mediated stabilization of the damaged nuclear membrane. We propose that this membrane-stabilizing response operates alongside established nuclear envelope repair mechanisms. Created in BioRender. Nylandsted, J. (2026) https://BioRender.com/sqxw4ca

## Discussion

Our findings identify ANXA4 as a $Ca^{2+}$-dependent regulator of NE integrity that acts through direct modulation of membrane mechanics. While responses to NE rupture have primarily been studied in the context of BAF-[7,8], LEM-domain–[9,23], and ESCRT-mediated repair pathways[5], our data support an additional, rapid membrane-centered response in which ANXA4 reinforces the damaged nuclear membrane. Rather than defining ANXA4 as a component of the canonical NE repair machinery, our findings support a model in which $Ca^{2+}$-dependent annexin recruitment modifies membrane mechanics and contributes to preservation of nuclear compartmentalization following injury. In this framework, ANXA4 functions as an acute membrane stabilizer that reinforces the NE following damage (Fig. 7).

We show that both ANXA4 and ANXA6 are recruited to the damaged NE, but with distinct spatial signatures. ANXA6 distributes broadly around the nuclear periphery, whereas ANXA4 displays stronger and polarized enrichment at the injured region. This difference is consistent with previously described functional specialization among annexins at the plasma membrane, where individual family members contribute distinct membrane-remodeling activities [13,14]. Our data extend this concept to the NE and suggest that different annexins may provide complementary mechanical functions depending on the geometry and extent of membrane damage. In particular, the localized accumulation of ANXA4 at the injured region is consistent with a role in focal membrane stabilization. Whether ANXA6 and other annexins cooperate with ANXA4 or perform distinct functions at damaged NE regions remains an important question for future studies.

Mechanistically, ANXA4 recruitment depends on $Ca^{2+}$ binding and trimer formation. Loss of $Ca^{2+}$ binding abolishes recruitment, whereas disruption of trimerization permits only transient membrane association without stable retention[14]. These findings support a two-step model in which $Ca^{2+}$ enables membrane binding, whereas trimerization promotes stable association of ANXA4 with the damaged membrane. In our experimental system, NE disruption alone was insufficient to trigger detectable ANXA4 accumulation, whereas concomitant plasma membrane disruption enabled robust recruitment. This suggests that ANXA4 engagement

requires a sufficiently strong $Ca^{2+}$ signal, with extracellular $Ca^{2+}$ influx providing this signal under the conditions used here. Whether comparable $Ca^{2+}$ elevations recruit ANXA4 to the NE under physiological forms of mechanical stress remains to be established.

Functionally, ANXA4 preserves NE integrity following injury. In Lamin A–deficient cells, which are intrinsically prone to NE rupture[22], ANXA4 preserves nuclear compartmentalization, whereas the trimerization-deficient mutant fails to do so. These results suggest that ANXA4 acts as a protective factor under conditions of compromised nuclear mechanics, potentially providing additional membrane reinforcement when the structural support provided by the nuclear lamina is reduced.

Importantly, our biophysical experiments provide evidence that ANXA4 directly alters membrane mechanics. Addition of recombinant ANXA4 to isolated nuclei reduces surface roughness and increases apparent nuclear stiffness, while in supported lipid bilayers ANXA4 increases resistance to mechanical failure without uniformly increasing bilayer stiffness. Together, these findings indicate that ANXA4 directly modifies membrane mechanics and increases resistance to mechanical failure, providing a physical basis for its membrane-stabilizing activity in cells.

More broadly, our findings raise the possibility that annexin-mediated membrane reinforcement represents a general mechanism for protecting mechanically compromised intracellular membranes. Given the shared $Ca^{2+}$-dependent membrane-binding properties of annexins, other family members may similarly contribute to membrane stabilization, either redundantly or through distinct functional specializations[17]. Whether ANXA4 performs similar stabilizing functions at other intracellular membrane compartments, including the endoplasmic reticulum, remains to be determined. Likewise, future work will be required to establish how ANXA4-mediated membrane stabilization interfaces temporally and functionally with established BAF-, LEM-domain- and ESCRT-dependent responses to NE rupture.

In summary, we identify ANXA4 as a rapid, $Ca^{2+}$-dependent membrane stabilizer that mechanically reinforces the NE following injury. $Ca^{2+}$-dependent membrane binding and trimerization promote stable ANXA4 association with damaged nuclear membranes, while ANXA4 preserves nuclear compartmentalization in cells and increases mechanical resistance

in isolated nuclei and reconstituted membranes. Our findings therefore reveal membrane reinforcement as a distinct component of the cellular response to NE rupture and establish a direct link between annexin assembly, membrane mechanics and nuclear integrity.

## Methods

### Cell culturing

The Lamin A (Lmna−/− and Lmna+/+) mouse embryonic fibroblasts (MEFs) were described previously [20] and cultured in Dulbecco's modified Eagle medium (DMEM) supplemented with 10% fetal bovine serum (FBS), 50 μg/ml streptomycin, and 50 U/ml penicillin[21]. Human breast adenocarcinoma cell line MCF7 were cultured in RPMI 1640 medium containing GlutaMAX (Thermo Fisher Scientific, 61870) and supplemented with 6% (v/v) heat-inactivated fetal bovine serum (FBS) (Thermo Fisher Scientific, 10270-106) and 0.25% (v/v) penicillin-streptomycin (Life Technologies, 11811-031). Cells were kept at 37°C in a humidified atmosphere with 5% $CO_2$ as a sub-confluent monolayer and were routinely tested for the presence of mycoplasma as analyzed by PCR and Hoechst staining. The MCF7 S1 clone was further modified using CRISPR/Cas9 technology to generate an ANXA4 knockout (CRISPR-A4KO) and control (CRISPR-Ctrl) cell line as previously described[14].
Live-cell imaging was performed in cell-imaging medium (CIM) consisting of RPMI 1640 medium without phenol red (Thermo Fisher Scientific, 32404014) supplemented with 2 mM GlutaMAX (Thermo Fisher Scientific, 35050038), 6% (v/v) FBS, 0.25% (v/v) penicillin-streptomycin and 25 mM Hepes (Sigma-Aldrich, H3375).

### Plasmid constructs and recombinant proteins

Expression plasmids containing human ANXA4 (OriGene, #RG203229) and ANXA6 (OriGene, #RG202086) with turboGFP (tGFP) were purchased from OriGene Technologies. ANXA4-tRFP had been generated previously[14]. In brief, ANXA4-tRFP had been generated by cloning ANXA4 (Origene, #RG203229) into the pCMV6-AC-tRFP vector (OriGene, #PS100034) using the restriction enzymes AsiSI and MluI[14]. ANXA4 mutants deficient in $Ca^{2+}$ binding (ANXA4Ca2+Mut) or deficient in trimer formation (ANXA4TriMut) had been generated previously [14]. pEGFP(C3)-Nup153 was a gift from B. Fahrenkrog (Addgene plasmid # 64268; http://n2t.net/addgene:64268; RRID:Addgene_64268)[24]. NLS-GFP was a kind gift from Jan Lammerding, Cornell University. tdTomato-LaminB1-10 was a gift from Michael Davidson (Addgene plasmid # 58107; http://n2t.net/addgene:58107;

RRID:Addgene_58107). Cells were transiently transfected with the indicated plasmids using Lipofectamine LTX (Invitrogen, 15338100) according to the manufacturer's instructions, omitting the Plus Reagent, and used for live-cell imaging experiments the day following transfection.

### *Recombinant ANXA4 protein generation*

Recombinant human ANXA4-sfGFP protein was produced and purified as previously described[14,25]. In brief, ANXA4 cDNA constructs were subcloned into the bacterial expression vector pETM11- SUMO3 (originally from EMBL Protein Expression and Purification Core Facility) with C-terminally tagged superfold GFP (sfGFP) and N-terminally tagged with a His6-tag and a SUMO3 domain. Recombinant ANXA4-sfGFP was produced by inducing the expression of the protein overnight at 18°C in BL21 (DE3) competent Escherichia coli cells using Isopropyl β-D-1 thiogalactopyranoside (IPTG). Next, cells were harvested by centrifugation at 4°C and lysed mechanically by sonication with the following settings: Pulse-on 10 s, pulse-off 5 s and duration 3 min. The lysate was centrifuged at 5.000xg for 10 min at 4°C and the supernatant was filtered (0.45µm). His6-tagged proteins were purified using Immobilized Metal-Affinity Chromatography (IMAC) with nickel-nitrilotriacetic acid (Ni-NTA) resins (Qiagen). The N-terminal His6-tag and SUMO3 domain were cleaved of by SUMOSpecific Protease 2 (SENP2) (200:1) followed by dialysis overnight at 4°C. The tag-cleaved proteins were further purified and separated using Fast Protein Liquid Chromatography (FPLC) on a Superdex 200 size-exclusion chromatography column (SuperdexTM 200, 10/300 GL, GE Healthcare Life Sciences). Protein fractions were collected and stored at -70°C until use.

## Live cell imaging

### *Laser injury*

Cells grown in MatTek imaging-culture dish were kept at 37°C in CIM. A 1-2 µm circular region of interest at the nuclear envelope of any intact single cell is selected and irradiated using a 355-nm ultraviolet ablation laser (Rapp OptoElectronic) with the following settings: 2.4% power, 200-Hz repetition rate, pulse energy > 60 µJ, and pulse length < 4 ns. Live-cell images were captured using an inverted microscope Eclipse Ti-E (Nikon) paired with an UltraVIEW VOX Spinning Disk (PerkinElmer and Volocity software (v6.3.1)). The Eclipse Ti-E was equipped with a Zeiss C Plan-Apochromat ×63/1.2 Water Korr objective and 488

nm and 555 nm lasers. Cells were imaged 4 to 10 s starting before injury and continuing for 5 min at 15 frames per minute (fpm) following injury. Control of hardware and intensity measurements were performed with PerkinElmer's Volocity software. Nuclear envelope integrity was measured by monitoring uptake of impermeable Hoechst 33258 dye (Sigma-Aldrich: 2.5µg/mL) as a change in fluorescence during the course of imaging for the dye.

***Injury using gold coated nanoparticles***

MCF7 CRISPR ANXA4KO cells were cultured in MatTek imaging dishes and transiently transfected with 3×NLS-GFP and ANXA4–tRFP 24 h before imaging. Sixteen hours before imaging, cells were loaded with 150-nm gold nanoparticles (AuNPs; BBI Solutions). Briefly, the AuNP stock suspension was vortexed for 10 s at maximum speed, and 100 µL was transferred to a microcentrifuge tube for each MatTek dish. Nanoparticles were pelleted by centrifugation at 1000 × *g* for 10 min, after which approximately 70% of the supernatant was removed. The pellet was resuspended in 100 µL culture medium by vortexing for 10 s at maximum speed, followed by sonication for 5 min at maximum amplitude. The suspension was vortexed again for 10 s, and 100 µL was added to each MatTek dish. Cells were incubated with AuNPs for 16 h at 37°C and 5% $CO_2$. Before imaging, cells were washed twice with Dulbecco's phosphate-buffered saline (PBS) lacking $CaCl_2$ and $MgCl_2$ (Thermo Fisher Scientific, 14190144), and the medium was replaced with CIM medium.

Laser-induced injuries were generated using a C-Trap optical tweezers system (LUMICKS), which combines optical trapping with confocal fluorescence imaging. A near-infrared trapping laser (1064 nm) was focused through a Nikon 60× water-immersion objective (CFI Plan Apo, NA 1.2). A piezoelectric stage was used to position the laser focus onto intracellular AuNPs located adjacent to either the plasma membrane or the nuclear envelope. AuNPs were exposed to the trapping laser for several seconds at powers between 100 and 200 mW, inducing localized heating and membrane damage. Simultaneously, confocal fluorescence images were acquired using excitation lasers at 488, 561, and 640 nm. Bright-field images were recorded in parallel at 60 frames $s^{-1}$ to enable real-time visualization of the injury site.

Fluorescence image analysis was performed using FIJI/ImageJ (National Institutes of Health, USA; Schindelin *et al*., 2012). Regions of interest were manually defined around injury sites or other intracellular reference regions. Mean fluorescence intensity and area measurements were obtained using built-in ImageJ tools over time. Images were exported and fluorescence intensity data were further analyzed in MATLAB (MathWorks).

**Western blot analysis**

Cells were lysed in Laemmli sample buffer (125 mM Tris (pH 6.7), 20% (v/v) glycerol, 140 mM SDS, 0.3 µM bromophenol blue) supplemented with 0.1 M dithiothreitol, cOmplete™, Mini Protease Inhibitor Cocktail (Roche, 4693124001) and PhosSTOP™ (Roche, 4906837001). Lysates were boiled for 5 min and separated by SDS-polyacrylamide gel electrophoresis using a 4-15% TGX$^{TM}$ Precast Protein Gel (Bio-Rad, 4561086), followed by blotting onto a nitrocellulose membranes (Bio-Rad, 1704158) using Trans-Blot Turbo transfer system. Novex Sharp Protein Standard (Invitrogen LC5800) was used to evaluate the molecular weights of proteins from the gels. After blocking in PBS containing 0.1% (v/v) Tween-20 (PBST) and 5% (w/v) BSA, membranes were cut in appropriate sizes for detection of proteins of interest and incubated overnight at 4°C with primary antibodies in PBST/0.1%$NaN_3$/5% BSA. Primary antibodies raised against human ANXA4 (R&D Systems #MAB4146, 1:200, RRID:AB_10892100) and Hsp90 (BD Biosciences, 610418; 1:4000, RRID:AB_397798) were used. Membranes were incubated for 30 min at room temperature with matching HRP-conjugated secondary antibodies ((Mouse IgG (rabbit) HRP-conjugated, Dako #P0450, 1:5000, RRID:AB_2630354). Chemiluminescent signals (Clarity Western ECL Substrate, Bio-Rad, 1705061) were detected with a luminescent image reader (ChemiDoc MP, Bio-Rad).

**Isolation of nuclei**

Nuclei were isolated using the Nuclei EZ Prep kit (Sigma-Aldrich, NUC101) according to the manufacturer's instructions with minor modifications. Prior to isolation, the optimal digitonin concentration was determined empirically. The selected concentration (15 µg/mL) induced plasma membrane damage that was repairable by approximately 95% of cells in $Ca^{2+}$-containing medium.

MCF7 cells grown in 150-mm culture dishes (70% confluency) were incubated with 15 µg/mL digitonin (Sigma-Aldrich) in culture medium for 15 min on ice with gentle rocking at 4°C. Cells were subsequently washed twice with 10 mL ice-cold PBS lacking $CaCl_2$ and $MgCl_2$. For cell lysis, 4 mL ice-cold Nuclei EZ lysis buffer was added to each dish, and cells were harvested by scraping and transferred to a 15-mL tube. Samples were vortexed at maximum speed for 10 s and incubated on ice for 10 min, followed by 10 passages through a

P1000 pipette tip and a second 10-s vortexing step. Nuclei were collected by centrifugation at 500 × *g* for 5 min at 4°C.

The supernatant was removed, and the nuclear pellet was resuspended in 0.5 mL ice-cold Nuclei EZ lysis buffer. After complete resuspension, 3.5 mL additional lysis buffer was added, and samples were incubated on ice for 10 min with gentle mixing every 3 min. The suspension was again triturated 10 times using a P1000 pipette tip, vortexed for 10 s, and centrifuged at 500 × *g* for 5 min at 4°C.

The resulting nuclear pellet was resuspended in 250 µL ice-cold Nuclei EZ storage buffer by repeated pipetting until a homogeneous suspension was obtained. The nuclei suspension was transferred to a fresh microcentrifuge tube and stored at −80°C until further use.

Purity and integrity of isolated nuclei were assessed by Hoechst 33342 staining (Merck Millipore, B2261) and bright-field microscopy. Only intact nuclei with preserved nuclear morphology were selected for subsequent analyses.

**Atomic Force Microscopy**

***Sample preparation for AFM experiments***

Immediately after thawing from storage at -80°C, nuclei were washed in PBS (no $Ca^{2+}$) (7 min at 700xg). Nuclei were then resuspended in PBS (no $Ca^{2+}$) and allowed to adhere to polyethyleneimine (PEI) coated glass slides for 1 h. The PEI coating method is described by Wang *et al.*[26]. After 1 h, nuclei coated coverslips were washed with PBS without $CaCl_2$ and $MgCl_2$, followed by 10 mM TRIS buffer (2-Amino-2- (hydroxymethyl)propane-1,3-diol), 140 mM NaCl, pH = 7.4.

***AFM imaging***

Atomic force microscopy (AFM) imaging was performed using a NanoWizard 4 instrument (JPK, Bruker) operated in alternating contact mode. Ultra-short cantilevers (USC-F0.3-k0.3, NanoWorld) with a nominal spring constant of 0.35 N $m^{-1}$ and a nominal tip radius of 10 nm (manufacturer specifications) were used throughout the study. All imaging was conducted using the lowest possible contact force to minimize sample deformation.

AFM imaging of PEI-adhered nuclei was performed in imaging buffer containing 10 mM Tris [2-amino-2-(hydroxymethyl)propane-1,3-diol], 140 mM NaCl, and 500 µM $Ca^{2+}$ (pH 7.4), in the presence or absence of 250 nM recombinant human ANXA4-sfGFP. Recombinant

ANXA4-sfGFP was added directly to the AFM fluid cell from a concentrated stock solution to achieve a final bulk concentration of 250 nM. Following protein addition, samples were allowed to equilibrate for 10 min before imaging. ANXA4-sfGFP fluorescence was monitored using a Nikon Ti2-E inverted microscope equipped with a 40× objective (Nikon ELWD S Plan Fluor, NA 0.6). Fluorescence excitation was provided by a white-light illumination system (CoolLED pE-300). Images were acquired with an ORCA-Flash4.0 V3 CMOS camera (Hamamatsu; 2048 × 2044 pixels) using NIS-Elements software (Nikon). Nuclei displaying median ANXA4-sfGFP fluorescence intensity within each sample were selected for AFM imaging. AFM images were processed using JPK Data Processing software (JPK, Bruker).

***Force measurements***

Force measurements were performed using a NanoWizard 4 AFM (JPK, Bruker) operated in contact mode with silicon nitride cantilevers bearing 1.5–3 μm colloidal probes (CP-PNPL-Au-A, NanoAndMore). All cantilevers were obtained from the same production batch. Photodetector sensitivity and cantilever spring constants were calibrated using the thermal noise method implemented in the JPK software. Measurements were conducted in buffer containing 10 mM Tris [2-amino-2-(hydroxymethyl)propane-1,3-diol], 140 mM NaCl, and 500 μM $Ca^{2+}$ (pH 7.4), in the presence or absence of 250 nM recombinant human (rh) ANXA4. Recombinant ANXA4 was added directly to the AFM fluid cell from a concentrated stock solution to achieve a final bulk concentration of 250 nM. Samples were equilibrated for 10 min following protein addition before force measurements were initiated. Nuclei isolated from MCF7 CRISPR ANXA4KO cells were randomly selected for analysis. For each nucleus, 16 force curves were acquired in a 4 × 4 grid covering a 250 × 250 nm region at the nuclear apex. Force curves were collected at a loading rate of 1 μm $s^{-1}$. To control for potential effects of prolonged $Ca^{2+}$ exposure on nuclear mechanics, all measurements were completed within 1 h of $Ca^{2+}$ addition. A total of 21 nuclei were analyzed in the absence of rANXA4 (control) and 20 nuclei in the presence of rANXA4. Each condition comprised nuclei obtained from three independent nuclear preparations. Force curves were analyzed using JPK Data Processing software (JPK, Bruker). The Hertz–Sneddon model was fitted to the force–indentation data to determine the apparent Young's modulus.

***Punchthrough measurements on supported lipid bilayers***

For punchthrough experiments on supported lipid bilayers in the presence or absence of ANXA4, AIOAI-B cantilevers (NanoAndMore) were used. These rectangular cantilevers have a nominal spring constant of 2.7 N $m^{-1}$ and a tip radius of <10 nm. Photodetector sensitivity and cantilever spring constants were calibrated using the thermal noise method implemented in the JPK software.

Force measurements were performed in 10 mM TRIS buffer (1.4 mM Trizma base, 8.5 mM Trizma hydrochloride, 140 mM NaCl, 2 mM $Ca^{2+}$, pH 7.4) in the presence or absence of 40 or 100 nM recombinant ANXA4-sfGFP protein. ANXA4-sfGFP was added from concentrated stock solutions to achieve the desired final concentration, and samples were allowed to equilibrate for 10 min before measurements were initiated.

Punchthrough measurements were acquired at a loading rate of 500 nm $s^{-1}$ and a sampling frequency of 7500 Hz. Force curves were collected in 7 × 7 grids spanning 10 × 10 μm areas at randomly selected locations on the supported lipid bilayer.

Force curves were preprocessed using JPK Data Processing software (version 8.0.183), including baseline subtraction and calculation of the vertical tip position. Punchthrough events were identified using the MATLAB function *findpeaks*. To be classified as a peak, a data point was required to exceed its neighboring points by at least 0.25 nN. Valleys were identified by mirroring the force curve about the x-axis and applying the same detection procedure. Because multiple punchthrough events could occur within a single force curve, detected peaks and valleys were paired sequentially, with the first peak assigned to the first valley, the second peak to the second valley, and so forth. Curves yielding negative peak-to-valley distances were excluded from further analysis.

***Preparation of supported lipid bilayers***

Supported lipid bilayers (SLBs) were prepared from 1-palmitoyl-2-oleoyl-sn-glycero-3-phosphocholine (POPC) and 1-palmitoyl-2-oleoyl-sn-glycero-3-phospho-L-serine (POPS) (Avanti Polar Lipids). Lipids were dissolved in methanol containing 0.5 mol% DiD oil (Thermo Fisher Scientific, D307) to a final total lipid concentration of 10 mM.

A droplet of lipid solution was deposited onto a freshly cleaved mica substrate and spin-coated at 3000 rpm for 40 s. The coated mica was subsequently placed in a vacuum desiccator overnight to ensure complete evaporation of the solvent. The dried lipid-coated mica was mounted in a liquid cell and hydrated with 10 mM TRIS buffer. The liquid cell was then incubated at 65°C for 1.5 h to promote bilayer formation.

Following hydration, excess upper bilayers were carefully removed by flushing the sample with preheated buffer while monitoring DiD fluorescence by microscopy, thereby ensuring measurements were performed on the primary bilayer directly attached to the mica substrate. After washing, samples were allowed to cool and equilibrate at room temperature for 1 h before use.

**Statistical analysis**

Statistical analyses were performed using GraphPad Prism (version 9.0.1; GraphPad Software). For fluorescence intensity time-course experiments, fluorescence values were first normalized and averaged at each time point for graphical presentation. Statistical comparisons between experimental groups were performed by calculating the area under the curve (AUC) for each individual cell and comparing AUC values using two-tailed *t* tests. Paired *t* tests were used when measurements were obtained from the same cell, whereas unpaired *t* tests were used for independent samples.

ACKNOWLEDGMENTS

This study was supported by the Danish Council for Independent Research, Natural Sciences (6108-00378A, 9040-00252B), the Novo Nordisk Foundation (NNF18OC0034936), and the Scientific Committee of the Danish Cancer Society (R90-A5847-14-S2). The spinning-disk confocal microscope used in this study was funded by the Danish National Research Foundation (DNRF125).

DATA AND MATERIAL AVAILABILITY

All data needed to evaluate the conclusions in the paper are present in the paper and/or the Supplementary Materials.

AUTHOR CONTRIBUTIONS

All authors contributed to the study, discussed the results, and reviewed and approved the final manuscript.

COMPETING FINANCIAL INTERESTS

All authors declare that they have no competing interests.

SUPPLEMENTARY FIGURES

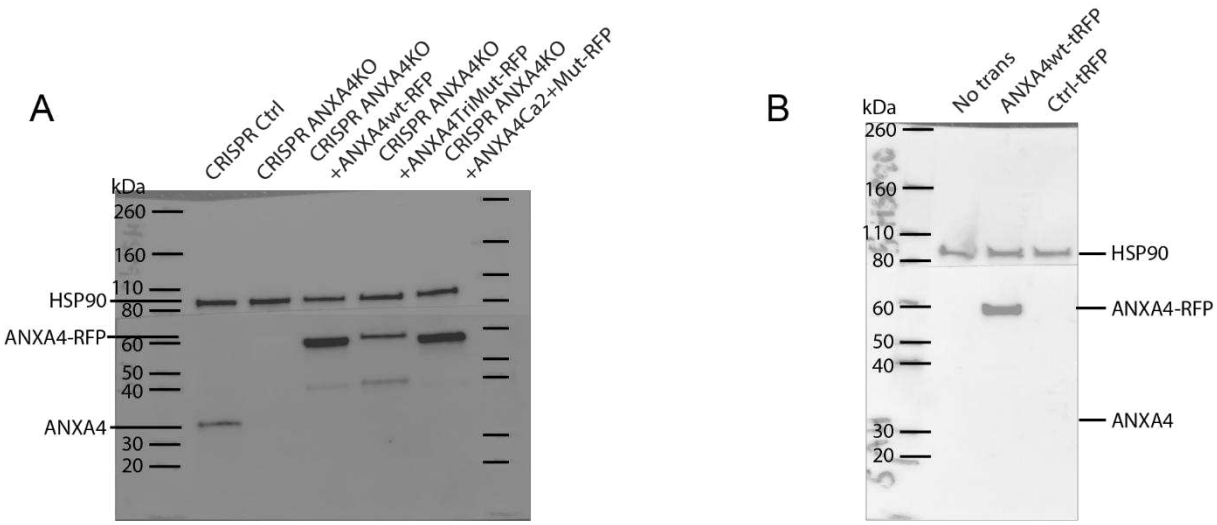



**Fig. S1.** (**A**) Complete immunoblot of lysates from MCF7 CRISPR control (Ctrl) and ANXA4KO cells following re-expression of ANXA4wt–RFP, ANXA4TriMut–RFP, or ANXA4Ca$^{2+}$Mut–RFP. Blots were probed with antibodies against ANXA4 and HSP90 **(loading control).** Related to Fig. 2B. (**B**) Original uncropped immunoblot showing ANXA4–tRFP expression following reintroduction into MCF7 CRISPR ANXA4 knockout cells. HSP90 serves as a loading control. Related to Fig. 4A

SUPPLEMENTARY MOVIE

**Movie S1:** Time-lapse video of MCF7 CRISPR ANXA4KO cell co-transfected with wildtype ANXA4–RFP and eGFP–NUP153 (nuclear pore complex) and subjected to injury at the nuclear envelope by focal UV-laser. Related to Fig. 2.

**Movie S2:** Time-lapse video of MCF7 CRISPR ANXA4KO cell co-transfected with the $Ca^{2+}$-binding–deficient mutant ANXA4$Ca^{2+}$Mut–RFP and eGFP–NUP153 (nuclear pore complex) and subjected to injury at the nuclear envelope by focal UV-laser. Related to Fig. 2.

**Movie S3:** Time-lapse video of MCF7 CRISPR ANXA4KO cell co-transfected with trimerization-deficient mutant ANXA4TriMut–RFP and eGFP–NUP153 (nuclear pore complex) and subjected to injury at the nuclear envelope by focal UV-laser. Related to Fig. 2.

REFERENCES


1. Caille, N., Thoumine, O., Tardy, Y. & Meister, J.J. Contribution of the nucleus to the mechanical properties of endothelial cells. *J Biomech* **35**, 177-87 (2002).
2. Lammerding, J. Mechanics of the nucleus. *Compr Physiol* **1**, 783-807 (2011).
3. Gruenbaum, Y., Margalit, A., Goldman, R.D., Shumaker, D.K. & Wilson, K.L. The nuclear lamina comes of age. *Nat Rev Mol Cell Biol* **6**, 21-31 (2005).
4. De Vos, W.H. et al. Repetitive disruptions of the nuclear envelope invoke temporary loss of cellular compartmentalization in laminopathies. *Hum Mol Genet* **20**, 4175-86 (2011).
5. Raab, M. et al. ESCRT III repairs nuclear envelope ruptures during cell migration to limit DNA damage and cell death. *Science* **352**, 359-62 (2016).
6. Denais, C.M. et al. Nuclear envelope rupture and repair during cancer cell migration. *Science* **352**, 353-8 (2016).
7. Young, A.M., Gunn, A.L. & Hatch, E.M. BAF facilitates interphase nuclear membrane repair through recruitment of nuclear transmembrane proteins. *Mol Biol Cell* **31**, 1551-1560 (2020).
8. Halfmann, C.T. et al. Repair of nuclear ruptures requires barrier-to-autointegration factor. *J Cell Biol* **218**, 2136-2149 (2019).
9. von Appen, A. et al. LEM2 phase separation promotes ESCRT-mediated nuclear envelope reformation. *Nature* **582**, 115-118 (2020).
10. Gerke, V. et al. Annexins-a family of proteins with distinctive tastes for cell signaling and membrane dynamics. *Nat Commun* **15**, 1574 (2024).
11. Bouter, A. et al. Annexin-A5 assembled into two-dimensional arrays promotes cell membrane repair. *Nat.Commun.* **2**, 270 (2011).
12. Bouvet, F. et al. Defective membrane repair machinery impairs survival of invasive cancer cells. *Sci Rep* **10**, 21821 (2020).
13. Boye, T.L. et al. Annexins induce curvature on free-edge membranes displaying distinct morphologies. *Sci Rep* **8**, 10309 (2018).
14. Boye, T.L. et al. Annexin A4 and A6 induce membrane curvature and constriction during cell membrane repair. *Nat Commun* **8**, 1623 (2017).
15. Florentsen, C.D. et al. Annexin A4 trimers are recruited by high membrane curvatures in giant plasma membrane vesicles. *Soft Matter* **17**, 308-318 (2021).

16. Berg Klenow, M. et al. Annexins A1 and A2 Accumulate and Are Immobilized at Cross-Linked Membrane-Membrane Interfaces. *Biochemistry* **60**, 1248-1259 (2021).
17. Raynal, P., Kuijpers, G., Rojas, E. & Pollard, H.B. A rise in nuclear calcium translocates annexins IV and V to the nuclear envelope. *FEBS Lett* **392**, 263-8 (1996).
18. Danielsen, H.M.D., Arastoo, M.R., Moreno-Pescador, G. & Bendix, P.M. A Thermoplasmonic Approach for Investigating Plasma Membrane Repair in Living Cells and Model Membranes. *J Vis Exp* (2024).
19. Ruhoff, V.T., Arastoo, M.R., Moreno-Pescador, G. & Bendix, P.M. Biological Applications of Thermoplasmonics. *Nano Lett* **24**, 777-789 (2024).
20. Sullivan, T. et al. Loss of A-type lamin expression compromises nuclear envelope integrity leading to muscular dystrophy. *J Cell Biol* **147**, 913-20 (1999).
21. Maynard, S. et al. Lamin A/C impairments cause mitochondrial dysfunction by attenuating PGC1alpha and the NAMPT-NAD+ pathway. *Nucleic Acids Res* **50**, 9948-9965 (2022).
22. Earle, A.J. et al. Mutant lamins cause nuclear envelope rupture and DNA damage in skeletal muscle cells. *Nat Mater* **19**, 464-473 (2020).
23. Gu, M. et al. LEM2 recruits CHMP7 for ESCRT-mediated nuclear envelope closure in fission yeast and human cells. *Proc Natl Acad Sci U S A* **114**, E2166-E2175 (2017).
24. Duheron, V., Chatel, G., Sauder, U., Oliveri, V. & Fahrenkrog, B. Structural characterization of altered nucleoporin Nup153 expression in human cells by thin-section electron microscopy. *Nucleus* **5**, 601-12 (2014).
25. Heitmann, A.S.B. et al. Phenothiazines alter plasma membrane properties and sensitize cancer cells to injury by inhibiting annexin-mediated repair. *J Biol Chem* **297**, 101012 (2021).
26. Wang, H., Wilksch, J.J., Lithgow, T., Strugnell, R.A. & Gee, M.L. Nanomechanics measurements of live bacteria reveal a mechanism for bacterial cell protection: the polysaccharide capsule in Klebsiella is a responsive polymer hydrogel that adapts to osmotic stress. *Soft Matter* **9**, 7560-7567 (2013).

## Supplementary Files

This is a list of supplementary files associated with this preprint. Click to download.

- MovieS2.mp4
- MovieS3.mp4
- MovieS1.mp4
- CoverLetter.pdf
- SUPPLEMENTARYFIGURE.pdf